Journal of
Materials Chemistry C

ROYAL SOCIETY
OF CHEMISTRY

PAPER

View Article Online
View Journal | View Issue

Cite this: *J. Mater. Chem. C*, 2021, **9**, 2793

Understanding the origin of broad-band emission in $CH_3NH_3PbBr_3$

Pronoy Nandi, †[ab] Chandan Giri ‡[a] and Dinesh Topwal *[ab]

Received 22nd October 2020,
Accepted 7th January 2021

DOI: 10.1039/d0tc05003b

rsc.li/materials-c

Broad-band emissions related to self-trapped excitons (STEs) in the sub-bandgap region in organic–inorganic hybrid perovskites and double perovskite crystals have drawn attention in recent times due to their potential in optoelectronic device applications. In this study, we have shown that the formation of STEs in $CH_3NH_3PbBr_3$ single crystals can be controlled using a suitable sample synthesis procedure. We have observed a broad-band emission (FWHM ~ 80 nm) for crystals whose crystallization is fast, whereas it was absent if we follow slow crystallization procedures. Using UV-Visible absorption spectroscopy, temperature-dependent photoluminescence (PL), time-resolved PL (TRPL), and dc magnetization studies, we concluded that defect-assisted extrinsic self-trapping is dominant here over the intrinsic self-trapping process and excess Pb atoms in interstitial positions are predominantly responsible for the extrinsic self-trapping process.

Introduction

Organic–inorganic lead halide hybrid perovskites are increasingly used in optoelectronic devices like photovoltaic cells,[1,2] bright light-emitting diodes,[3] photodetectors,[4] lasers,[5] *etc.* due to their remarkable optoelectronic properties like high carrier mobility,[6] high photoconversion efficiency,[7] tunable bandgap (with composition),[8] long charge carrier diffusion length[9] and rare trap density.[10] However, defects in these systems can greatly influence the luminescence efficiency, electrical conductance, minority carrier lifetime, and other key aspects of device performance. It was observed that vacancies, self-interstitials and antisites have deleterious effects on the performance of a laser, LED and photodetector.[11–13] Thus, to enhance the device performance, it is essential to optimize the sample growth process, understand the origins of defects and reduce the same.

The synthesis of organic–inorganic hybrid halide perovskite crystals was first reported by Weber in 1978 by the solution temperature lowering (STL) method where methylammonium (MA) and lead-acetate were dissolved in hydrohalide acid, heated at 100 °C and subsequently cooled to 45 °C resulting in millimeter-sized crystals.[14] Subsequently by judiciously changing the precursors (use methylammonium halide instead of methylammonium and hydrohalide acid)[15,16] and varying the growth rate,[17] pyramidal, rhombohedral or cuboid sized crystals were obtained. Reduced structural imperfections, and a variety of morphologies and polymorphic forms are the major advantages of this process. However, the slow growth rate and the probability of solvent inclusion in the sample are the main disadvantages.

Another suitable method of crystal growth is the inverse temperature crystallization (ITC) method wherein the solubility of organic–inorganic metal halides in particular solvents is high at room temperature but decreases rapidly with increasing temperatures. γ-Butyrolactone (GBL), *N*,*N*-dimethylformamide (DMF) and dimethylsulphoxide (DMSO) were chosen for ITC growth of $CH_3NH_3PbI_3/CH(NH_2)_2PbI_3$, $CH_3NH_3PbBr_3/CH(NH_2)_2PbBr_3$ and $CH_3NH_3PbCl_3$ single crystals, respectively, and by setting a high temperature of the heating bath, single crystals quickly precipitated.[18–22] Liu *et al.* have grown the largest single crystals of $CH_3NH_3PbI_3$ so far (two-inch) using this method.[23] Because of a faster growth rate ($\sim$1 mm^3 h^{-1}), this method can be adopted for commercial purposes, but structural imperfection and solvent corrosion might arise due to the high growth temperature which deteriorates the crystalline quality of these perovskites. However, a novel space-limited ITC method has recently been developed to fabricate large (120 cm^2) single crystal films of $CH_3NH_3PbBr_3$ on FTO glass for narrow bandgap-photodetectors.[24]

D. Shi *et al.* proposed an alternative strategy to synthesize single crystals of metal halide perovskites using the anti-solvent vapor assisted crystallization (AVC) method.[25] This method is used to synthesize materials which are highly soluble in one solvent (good solvent) but have poor solubility in other solvents (bad solvent) and diffusion of a suitable bad solvent vapor into the precursor solution results in high-quality crystals.[26,27]

---

[a] *Institute of Physics, Sachivalaya Marg, Bhubaneswar 751005, Odisha, India*

[b] *Homi Bhabha National Institute, Training School Complex, Anushakti Nagar, Mumbai 400094, India. E-mail: dinesh.topwal@iopb.res.in*

† Present address: Department of Energy Science, Sungkyunkwan University, Suwon 16419, Republic of Korea.

‡ Present address: Department of Chemistry and Biochemistry, The University of Alabama, Tuscaloosa, Alabama, 35487-0336, USA.

Single crystals of metal halide perovskites using the AVC method were synthesized using toluene and dichloromethane (DCM) as antisolvents.[28–30] The proposed room temperature crystallization technique is important in particular for thermally sensitive samples, where organic groups are present. Furthermore, the presence of an antisolvent changes the solvent activity of the solution which has a more profound effect on the morphology and polymorphic form than that of ITC and STL methods, whereas, the use of additional raw material (*i.e.*, antisolvent) might create problems in the purity of crystals and may also enhance the capital cost.

Though several groups have synthesized and characterized[14–23,25–30] single crystals of metal halide perovskites using the above-discussed methods, no comparative study is available, focusing on the crystallographic and spectroscopic nature of the obtained samples prepared by different methods. In this report, a comparative study of heat capacity, room temperature powder X-ray diffraction (XRD), room temperature absorbance and temperature-dependent photoluminescence (PL) on single crystals of $CH_3NH_3PbBr_3$ synthesized by STL, ITC, dichloromethane (DCM) and ethylacetate (EA) diffused AVC methods has been carried out. Samples grown by these four methods are found to be crystallographically identical, however, discrepancies are observed in their optical response. A broad-band emission spectrum between 600 nm and 750 nm was observed in the crystals grown by rapid crystallization techniques like STL, ITC and DCM diffused AVC methods, whereas this broad-band emission spectrum is absent in the EA diffused AVC method (slow crystallization technique). The large Stokes shift, broadband emitting spectrum with full width at half maximum (FWHM) larger than 80 nm and high recombination time ($\sim$0.48 μs) indicated that these broad-band emissions are related to self-trapped excitons (STEs).[13] Short-range lattice distortion due to the localization of free excitons (FEs) is responsible for the formation of STEs and can be divided into two types: (a) intrinsic and (b) extrinsic self-trapping.[31–34] Transient distortions of the lattice create intrinsic self-trapping, example: structural distortion in $InBr_6$ octahedra in the lead free indium-based counterparts,[35,36] while lattice distortion due to permanent defects in materials like doping or alloying causes the extrinsic self-trapping, example: Pb or Br vacancies in interstitial positions.[37]

In this article, we have made a comparison of formation energy calculations with the experimentally obtained energy levels and suggest that excess Pb atoms in interstitial positions are predominantly responsible for the extrinsic self-trapping process which is supported by dc-magnetization studies.

Results and discussion

Powder X-ray diffraction (PXRD) and heat capacity measurements were performed on all four $CH_3NH_3PbBr_3$ samples to assess their structure and phase purity. Fig. 1(a) shows that samples are crystalline in nature and diffraction peaks of all four samples appear at the same 2θ position, (indexed in the figure), which match well with those of the $CH_3NH_3PbBr_3$ perovskite with a cubic phase structure ($Pm\bar{3}m$ space group).[30,38]

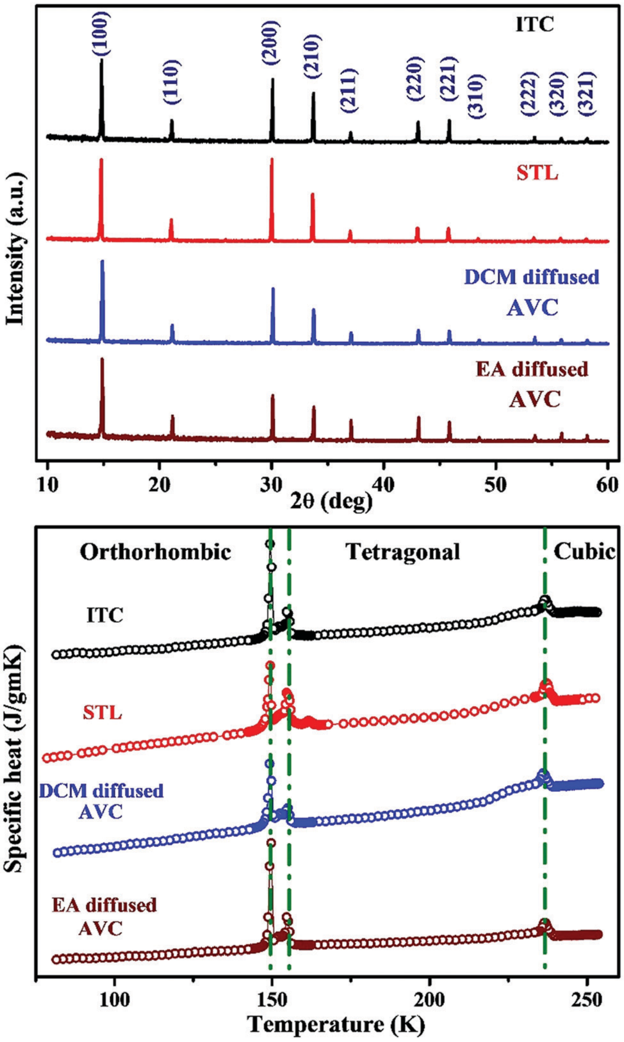

Fig. 1 Room temperature powder X-ray diffraction patterns (upper panel) and heat capacity (lower panel) of $CH_3NH_3PbBr_3$ grown by ITC, STC, DCM and EA diffused AVC methods.

Sharp and well-resolved diffraction peaks indicate that the crystallite size of $CH_3NH_3PbBr_3$ grown by the above-mentioned techniques is quite large and is free from lattice strain. Temperature-dependent heat capacity measurements were performed to identify the phase transition temperatures (Fig. 1(b)).[39] It was observed that all four samples undergo crystallographic phase transitions at the same temperatures. With the decrease of temperature from 280 K to 70 K, sharp anomalies were observed at 236.9 K, 154.6 K and 149.3 K for all the samples indicating a change in internal energies arising from the crystallographic phase transition of the samples. A comparison with previous reports suggest that all four samples undergo a crystallographic phase transition from cubic to tetragonal (I), tetragonal (I) to tetragonal (II) and tetragonal (II) to orthorhombic at 236.9 K, 154.6 K and 149.3 K, respectively.[40] From these observations we might conclude that all the four samples are crystallographically identical.

The optical properties of all four as-synthesized samples were investigated using steady-state absorption and PL studies.

Fig. 2 depicts the room temperature UV-visible absorption spectra of $CH_3NH_3PbBr_3$ synthesized *via* ITC, DCM diffused AVC, STL and EA diffused AVC techniques. Each spectrum was acquired from a pellet (diameter of 10 mm) made by crushing an equal amount (120 mg) of single crystals of $CH_3NH_3PbBr_3$ and consists of three broad features; (i) a sub-bandgap absorption at low energy (600 nm and above), (ii) a strong and sharp peak at 556 nm (2.23 eV) followed by (iii) band-edge transitions which start from 506 nm (2.45 eV).[39,41] Steeper band edges of $CH_3NH_3PbBr_3$ suggest that it is a direct bandgap semiconductor with ordered nature. Apart from dual transitions at 506 nm and 556 nm (with an error bar of ±2 nm) a broad hump between 600 nm and 750 nm was observed for samples synthesized by ITC, STL and DCM diffused AVC methods. Furthermore, the relative absorbance of the broad hump was maximum for samples grown by the ITC method, followed by DCM diffused AVC and STL methods, respectively. In contrast, no broad absorbance peak was observed for the sample grown by the EA diffused AVC method, suggesting that the optical response can vary depending on the sample synthesis conditions.

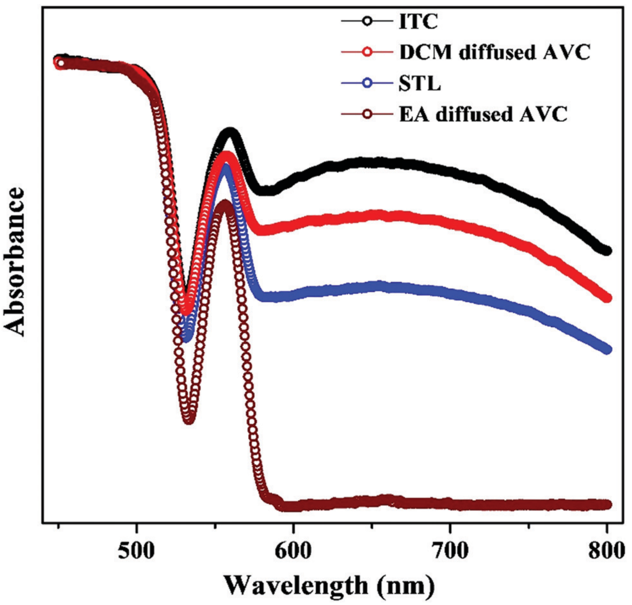

Fig. 2 Room temperature UV-VIS absorbance spectra of four $CH_3NH_3PbBr_3$ samples grown by ITC, STC, DCM and EA diffused AVC methods.

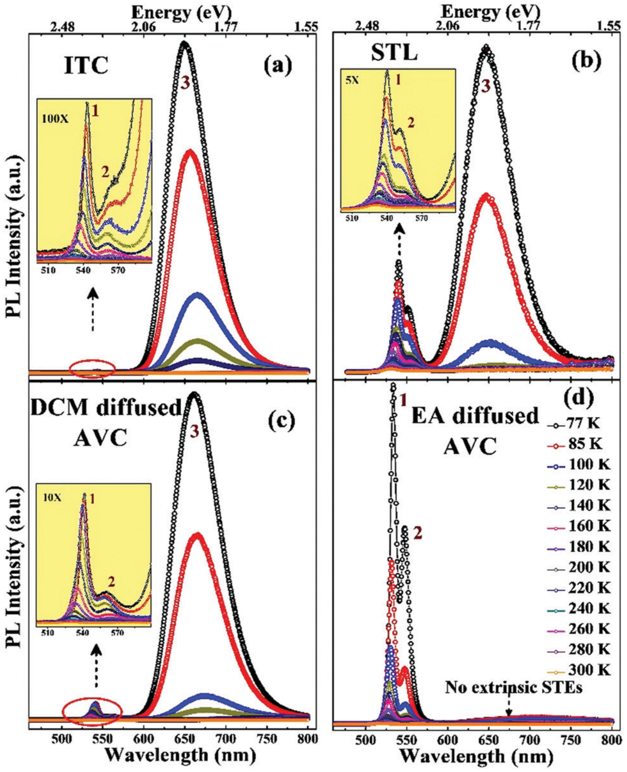

Fig. 3 Temperature-dependent photoluminescence spectra of $CH_3NH_3PbBr_3$ grown by (a) ITC, (b) STC, (c) DCM diffused and (d) EA diffused AVC method. Inset shows the variation of first two peaks with temperature.

Fig. 3 shows the temperature-dependent (77 K to 300 K) steady-state PL spectra of $CH_3NH_3PbBr_3$. The overall features of the presented PL spectra from samples synthesized using different processes are somewhat similar and can be broadly characterized by three peaks marked as 1, 2, and 3 in the figures, but with different intensities. For the sample grown by the ITC method three PL emission peaks were observed (i) peak-1 at 543.5 nm, (ii) peak-2 at 561 nm and (iii) peak-3 at 649 nm at 77 K, which are consistent with the literature.[42–44] Also, as the temperature is increased, peak-1 is blue-shifted, while peak-2 is red-shifted continuously to 529.5 nm and 573.5 nm, respectively, at room temperature (300 K), and peak 3 is red-shifted. It may here be noted that peak 3 shows strong temperature dependence and considerable FWHM as compared to peak 1 and peak 2. This observation is consistent for samples grown by all 4 methods. The bandgap energy of most of the semiconductors tends to decrease (red shift) with increasing temperature and at higher temperature, interatomic bonds are weakened and weaker bonds mean less energy required to send an electron in the conduction band. However, the blue-shifting behavior of peak-1 in the hybrid perovskite is inconsistent with that of traditional semiconductors and can be explained using the Varshni model where the temperature coefficient of bandgap (dE_g/dT) can be expressed as:[39,45]

$$\left(\frac{\mathrm{d}E_\mathrm{g}}{\mathrm{d}T}\right)_p = \left(\frac{\mathrm{d}E_\mathrm{g}}{\mathrm{d}T}\right)_v + \left(\frac{\mathrm{d}E_\mathrm{g}}{\mathrm{d}\ln(v)}\right)_T \left(\frac{\mathrm{d}\ln(v)}{\mathrm{d}T}\right)_p \tag{1}$$

Here the first term represents the electron–phonon coupling through the deformation coupling, which represents a decrease in bandgap with an increase of temperature and the second term is the lattice dilation term which causes the increase in the bandgap with temperature. It is suggested that the blue shifting nature of peak-1 arises because of valence band maxima stabilization due to lattice dilation with an increase in the temperature.[39]

The origin of dual emission in PL spectra (peak-1 and peak-2) is a widely debated topic in this series of compounds with no consensus so far; few authors claim it to be surface and bulk effect,[18,19] some refer it to be arising from bound and free exciton emission,[42] while others believe that tetragonal inclusions in the low temperature are responsible.[43] However, based on our experiments and band structure calculations,[46] we believe that methylammonium orientations inside the $PbBr_6$ octahedra can result in two closely spaced minima in free energy *vs.* molecular orientation plot.[47] The electronic structures associated with these two configurations confirm a small shift in the valence band and no shift in the conduction band and these closely spaced valence bands might be responsible for dual transitions in hybrid perovskites.[39,44]

The results of the temperature-dependent steady-state PL spectra of the samples grown by STL and DCM diffused AVC methods are depicted in Fig. 3(b) and (c), respectively, and are similar to the samples grown by the ITC method (Fig. 3a). However, the relative intensity of peak-3 (at 77 K) w.r.t. peak-1 is maximum for the sample grown by the ITC method and is minimum for the sample grown by the STL method. By looking at the position of peak 3 in the energy level diagram, one can assume it to be originating from some deep level trap states which appears at the interband positions and originates due to the rapid growth rate at high temperature and fast diffusion by the low boiling point solvent (DCM: 39.6 °C). A similar observation was made in the UV-visible absorbance study of the corresponding samples (Fig. 2). Furthermore, it is important to note that peak-3 is absent at all temperatures for the samples grown at room temperature by high boiling point antisolvent diffusion (EA: 77.1 °C) methods, where the growth rate is relatively lower. Thus, in conclusion, broadband peak-3 was observed when the sample was synthesized by rapid crystallization methods (ITC, STL, and DCM diffused AVC methods), while no broad peak was observed for samples grown by the relatively slow crystallization method (EA diffused AVC method).

The broad emission/absorption in the midgap region for semiconductors and insulators is best described in terms of intrinsic self-trapping of electrons and excitons (STEs).[31–34] Additionally, it has been suggested that the presence of intrinsic defects or impurity atoms in the crystal can add further inhomogeneity to the excited-state potential surface, leading to escalation of the broad mid-bandgap emission response.[37] Accordingly, STEs as well as carrier trapped permanent lattice defects are believed to be responsible for broadband white light emission in zero dimensional perovskites like $(C_4H_{14}N_2)_2In_2Br_{10}$,[36] $(Cs_2InBr_5{\cdot}H_2O)$,[35] two dimensional hybrid perovskites like ((N-MEDA)[$PbBr_4$] (N-MEDA = N^1-methyl ethane-1,2-diammonium),[48] (EDBE)[PbX_4] (EDBE = 2,2′ (ethylenedioxy)bis (ethylammonium); X = Cl and Br)),[49] in double perovskites like $Cs_2AgInCl_6$,[50] $Cs_2NaInCl_6$,[51] Cs_4SnBr_6, *etc.*[52] and in ion (Yb^{3+}/Er^{3+}) doped all inorganic hybrid perovskite $CsPb(Br/Cl)_3$.[13] Similar to our steady state photoluminescence observations, Priante *et al.*,[42] Fu *et al.*[44] and Shi *et al.*[53] also observed broad-band PL emission between 560 nm and 690 nm at low temperature (77 K) for $CH_3NH_3PbBr_3$, which disappeared above 180 K. Using variable fluence and excitation (below band-edge) dependent steady state and time resolved PL studies, they ascribed this feature (appearing as peak 3 in our case) to self-trapped excitonic emission. Furthermore, careful observation of the present data reveals that excitonic peak positions (peak 1 and 2) show a redshift of 41–45 meV for ITC, 32–35 meV for the DCM diffused AVC and 27–28 meV for the STL method grown sample compared to the EA diffused AVC sample throughout the temperature region. This result clearly indicates that the local configurations of trap states and electronic properties are quite sensitive to their charge states introduced by the permanent lattice defects or e-STEs and can result in the shifting of valence band maxima (VBM) or conduction band minima (CBM).[54]

Time-correlated single-photon counting (TCSPC) of peak-1 and peak-3 (presented in Fig. 4) could shed some light on the recombination time (of electrons and holes) and help in identifying permanent lattice defects or e-STE results of the same for samples prepared by the ITC method. The lifetime of the energy levels responsible for peak-1 and peak-2 (not shown here) is relatively small (ns range), while, that of peak-3 is three orders of magnitude higher in μs range confirming a different origin of peak-3. The recombination lifetime of $CH_3NH_3PbBr_3$ was determined by measuring PL decay at the emission peak wavelengths and the curves are fitted with the biexponential function of time (t) given by:

$$I(t) = I_1 \exp^{-t_1/\tau_1} + I_2 \exp^{-t_2/\tau_2} \tag{2}$$

where τ_i is the decay time and I_i is the weight factor of each decay channel. The peak-1 fitting yielded following parameters t_1 = 17.8 ns with 59.32% weight% and t_2 = 3.5 ns with 40.68% weight%. Here, slow (17.8 ns) and fast (3.5 ns) recombination times are assigned as bulk and surface recombination.[18,22,39] In contrast, the lifetime of energy levels associated with peak-3 was as large as t_1 = 0.48 μs with 57.12% weight% and t_2 = 3.32 μs with 42.88% weight%, suggesting that the transitions responsible for emission of peak-3 originate from defect levels.

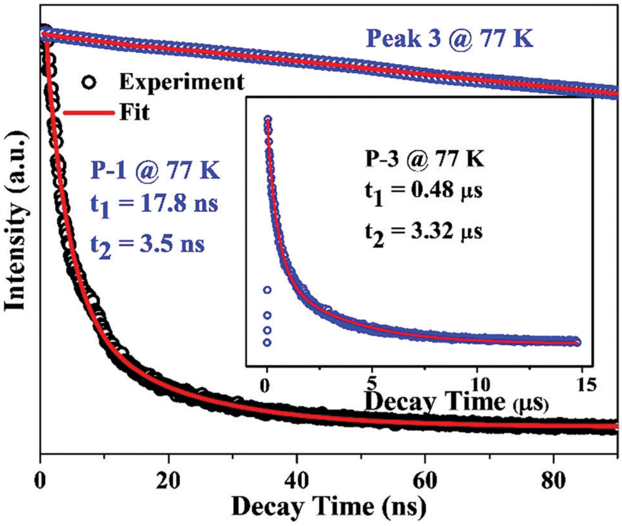

Fig. 4 Time correlated single photon counting (TCSPC) data corresponding to 650 nm and 531 nm (Inset) emission peaks at 77 K of $CH_3NH_3PbBr_3$ grown by the ITC method. *Y*-Axis is normalized at t = 0 ns and presented in log-scale for better visualization. Hollow dots represent the experimental data.

Depending on the location of the energy states in the band diagram, defect states might be characterized as shallow or deep levels. Shallow defects have energy levels within few tens of meV from respective band edges, whereas deep level defects reside within the middle third of the bandgap. Alternatively, deep levels are associated with highly localized wave functions whereas shallow level wave functions are as extended as the far-reaching coulomb potential. Based on these definitions, almost all dominant defects in $CH_3NH_3PbBr_3$ can be characterized from shallow levels except the following cases (deep level effects):[55–57] (i) CH_3NH_3(MA), Pb, Br vacancies (V_{MA}, V_{Pb}, V_{Br}), (ii) MA, Pb, Br interstitial (MA_i, Pb_i, Br_i), (iii) MA on Pb (MA_{Pb}) and Pb on MA (Pb_{MA}) cation substitution and (iv) MA on Br (MA_{Br}), Pb on Br (Pb_{Br}), Br on MA (Br_{MA}), Br on Pb (Br_{Pb}) antisite substitutions. Formation energy calculations reveal that MA_i, Pb_{MA}, V_{Br} and MA_{Br} are shallow donors whereas Br_i, MA_{Pb}, V_{MA}, and V_{Pb} are shallow acceptors which are not responsible for the observed midgap defect states. The remaining four defects Pb_i, Pb_{Br}, Br_{MA} and Br_{Pb} produce deep levels in the bandgap of $CH_3NH_3PbBr_3$.[55] Formation energy calculations reveal that Pb_i and Pb_{Br} levels are situated nearer the conduction band, whereas, Br_{MA} and Br_{Pb} exist closer to the valence band, and are responsible for the interband transition.

For a better understanding of the defect states, we substituted Br ion sites with Cl and synthesized single crystals of $CH_3NH_3PbCl_3$ *via* ITC and EA diffused AVC methods. The steady-state PL spectra at 77 K of both the Cl replaced samples are shown in Fig. 5. Here too we observe two peaks at 403 nm (peak-1) and 410.5 nm (peak-2) for both the samples and an additional peak at 641.5 nm (peak-3) for the sample synthesized by the ITC method while peak-3 was absent for the sample synthesized by the EA diffused AVC method. This result is similar to the one from $CH_3NH_3PbBr_3$ thereby confirming that halogen atoms do not participate in deep level defect formation in metal halide perovskite crystals. These experimental observations suggest that point defects due to self-doping of Pb atoms are responsible for the creation of the midgap defect states evidenced here. Furthermore, formation energy calculations predict that unipolar self-doping of Pb at interstitial positions can create interband defect states,[55] while density functional theory (DFT) calculations also predict mid-gap defect states in the calculated absorption spectra of $CH_3NH_3PbI_3$.[58] If the interstitial Pb atoms are indeed responsible for defect states of methylammonium lead halide samples, then uncompensated spins of Pb can align in the applied magnetic field direction like Mn-doped $CH_3NH_3PbBr_3$ micro-rods.[59]

Magnetization measurements (*M vs. H*) as a function of the applied field were performed on all $CH_3NH_3PbBr_3$ samples at 100 K and 300 K, which are presented in Fig. 6. It is observed that the sample synthesized by the EA diffused AVC method is diamagnetic in nature with susceptibility $\chi = -4.43 \times 10^{-9}$ (inset of Fig. 6) which is consistent with the literature reports.[59,60] However, other three samples synthesized by STL, DCM diffused AVC and ITC methods show a mixture of para and ferromagnetic behavior. It is interesting to observe

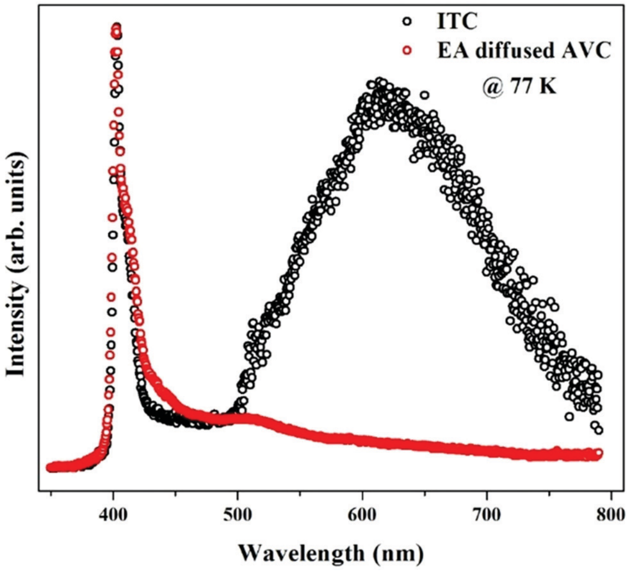

Fig. 5 Temperature-dependent photoluminescence spectra of $CH_3NH_3PbCl_3$ grown by ITC and EA diffused AVC methods at 77 K.

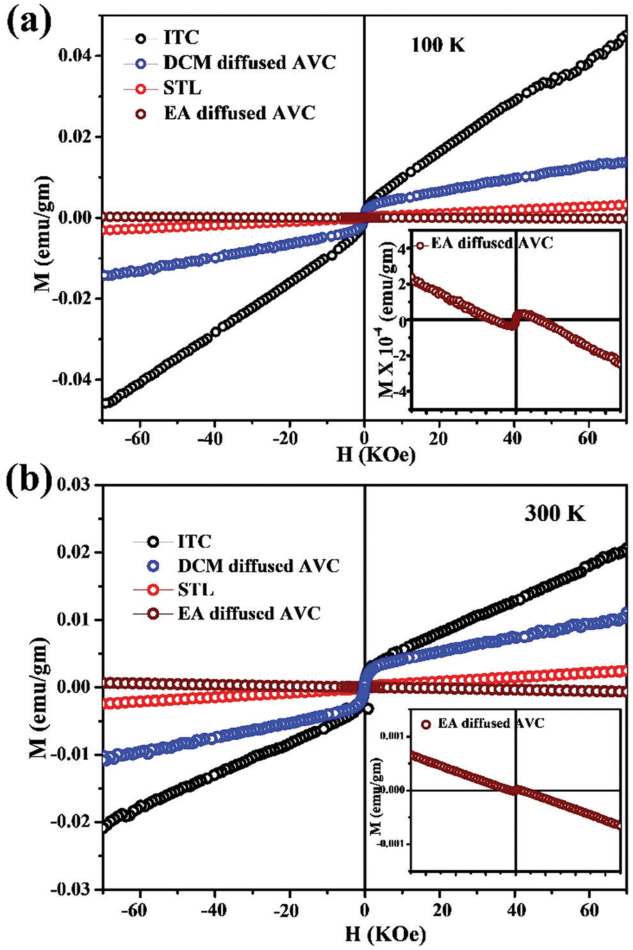

Fig. 6 *M–H* loops of $CH_3NH_3PbBr_3$ grown by ITC, STC, DCM and EA diffused AVC methods taken at (a) 100 K and (b) room temperature (300 K). Inset shows the diamagnetic behavior of $CH_3NH_3PbBr_3$ grown *via* the EA diffused AVC method.

that the magnetic moment is maximum for the sample grown by the ITC method (0.039 emu g^{-1} and 0.018 emu g^{-1}), followed by the DCM diffused AVC method (0.013 emu g^{-1} and 0.009 emu g^{-1}) and the STL method (0.003 emu g^{-1} and 0.002 emu g^{-1}) at a magnetic field of 60 kOe for 100 K and 300 K, respectively. The observed trend in the magnitude of magnetization is directly proportional to the number of interstitial Pb atoms (point defects: interstitial and vacancy) and is consistent with conclusions from PL results. The observed phenomena (Fig. 6) in $CH_3NH_3PbBr_3$ can hence be best described as defect induced magnetism as observed in graphite,[61] graphene,[62] and ZnO.[63] Recently, Sil *et al.* observed defect-induced ferromagnetism at room temperature in the $CH_3NH_3PbI_3$ system and suggested that the origin of ferromagnetic ordering in this material is due to atomic defects.[64] Náfrádi *et al.* also observed ferromagnetic behavior in $MAPbI_3$ after substituting Pb^{2+} with Mn^{2+} and fabricated optically tuned magnetic switches.[65] Thus, we believe that defect states present in the sample are responsible for the deviation from the expected diamagnetic behavior and that the number of interstitial Pb atoms in the system is the highest for samples grown by the ITC method and minimum for the samples grown by the STL method and is almost negligible for the case of the sample grown by the EA diffused AVC method. This interesting magnetic behavior for a direct bandgap semiconductor like $CH_3NH_3PbBr_3$ where magnetism can be induced and controlled by the amount of defects opens up new avenue for utilizing organic–inorganic halide perovskites for spintronic applications as well.

Conclusions

In summary, we have carried out an in-depth comparative study of the structural, optical and magnetic properties of $CH_3NH_3PbBr_3$ grown by ITC, STL, DCM and EA diffused AVC methods through powder XRD, heat capacity, room temperature UV-VIS and temperature-dependent PL spectroscopy as well as *M–H* studies. Identical PXRD patterns and heat capacity confirm the phase purity and the presence of three crystallographic phase transitions in all four samples synthesized by different techniques. However, the presence of a broad peak between 600 nm and 700 nm was observed in the sub-bandgap region (bandgap of $CH_3NH_3PbBr_3$ is approx. 506 nm) in the room temperature absorption and temperature-dependent PL studies in case of samples grown by ITC, STL and DCM diffused AVC methods, which was absent in the sample grown by the EA diffused AVC method. The time-resolved PL study confirms that the lifetime associated with this broad peak is higher ($\sim\mu$s) than that of band-edge transitions ($\sim$ns). A comparison with the formation energy calculations confirmed that excess Pb atoms in interstitial positions create defect levels for the samples whose growth rate is high. This observation was also confirmed by dc magnetization studies. Thus, a novel approach to synthesize defect-free crystals is put forth which will be useful to fabricate optoelectronic devices using metal halide perovskite single crystals.

Experimental section

Materials

All chemicals were purchased from Sigma-Aldrich and used as received without further purification: hydrobromic acid (HBr; 48 wt% in water), methylamine (CH_3NH_2; 40 wt% in water), $PbBr_2$ (99.99%), PbI_2 (99.99%), and γ-butyrolactone (GBL; 99.9%).

Synthesis of CH_3NH_3Br

Single crystals of CH_3NH_3Br were synthesized by reacting CH_3NH_2 and HBr in a molar ratio of 1.2 : 1. HBr was added dropwise into CH_3NH_2 in a flask under a nitrogen atmosphere in an ice bath for 3 hours; the resulting solution was evaporated at 60 °C in a rotary evaporator to remove the unreacted solvent and white crystals of CH_3NH_3Br were obtained.

Synthesis of $CH_3NH_3PbBr_3$ single crystals

Method-1: Inverse temperature crystallization (ITC) method. 0.367 g lead(II) bromide (1 mM) and 0.111 g methylammonium bromide (1 mM) were dissolved in 10 ml *N*,*N*-dimethylformamide (DMF) and the precursor solution was kept at 80 °C. After 3 h nice orange-colored single crystals of $CH_3NH_3PbBr_3$ were grown.

Method-2: Solution temperature lowering (STL) method. In this technique, we have reduced the temperature of precursor solution (same as method-1) from 100 °C to room temperature over 48 h as reported earlier. This is the most common and traditional way to synthesize $CH_3NH_3PbBr_3$ perovskite single crystals. It is also observed that crystallization increases at around 80 °C.

Anti-solvent vapor assisted crystallization (AVC) method

We know that the solubility of a compound in one solvent (good solvent) decreases due to the slow incorporation of another solvent (bad solvent) in which the solute is not soluble (an anti-solvent). This can be done in two ways; one is by direct contact between the saturated solution and the anti-solvent ("layering") and other by allowing the vapors of the anti-solvent to slowly diffuse into a saturated solution. In this method, ethyl acetate (EA) and dichloromethane (DCM) vapors are used to reduce the solubility of the solute.

Method-3: Dichloromethane (DCM) diffused AVC method. In this method, the precursor solution (same as method-1) filled vial was kept in a DCM environment and orange crystals were grown within 1–2 days.

Method-4: Ethyl acetate (EA) diffused AVC method. In order to achieve very slow crystallization, we have taken a high boiling point solvent (ethyl acetate: 77.1 °C). Then, the vial containing the $CH_3NH_3PbBr_3$ precursor solution (same as method-1) was kept in an EA environment. With slow diffusion of EA into the solution, nice orange crystals were grown within 8–10 days.

Characterization techniques

X-Ray powder diffraction of all samples was performed by using a Bruker D8 Advance diffractometer using Cu K_α

radiation (λ = 1.34 Å) to confirm the phase purity of all four samples. The temperature dependence of specific heat of all four samples was recorded using a Physical Property Measurement System (PPMS) Evercool II, from Quantum Design, USA. Heat capacity measurements were performed in the temperature range between 70 K and 300 K. The optical absorption spectra were recorded using an ultraviolet-visible-near-infrared spectrophotometer (Shimadzu, 3101PC) in the wavelength range of 400–800 nm. Temperature-dependent photoluminescence (PL) spectra of all the samples were recorded in the temperature range of 77 K to 300 K using a FL920 spectrometer from Edinburg instruments with an excitation energy of 325 nm. Time-resolved PL experiments were performed on the same FL 920 spectrometer by means of time-correlated single-photon counting (TCSPC). For both the measurements, samples were mounted on a copper plate in a cryostat and cooled by liquid nitrogen. The dc-magnetization measurements of all four samples were performed at 300 K using a PPMS system equipped with VSM head from Quantum Design, USA.

Conflicts of interest

There are no conflicts to declare.

Acknowledgements

DT would like to acknowledge SERB, DST, India (funding under project file no. CRG/2020/003108) for financial support.

References

1 J. Y. Kim, J.-W. Lee, H. S. Jung, H. Shin and N.-G. Park, *Chem. Rev.*, 2020, **120**, 7867–7918.

2 P. Yadav, D. Prochowicz, E. A. Alharbi, S. M. Zakeeruddin and M. Grätzel, *J. Mater. Chem. C*, 2017, **5**, 7799–7805.

3 Q.-W. Liu, S. Yuan, S.-Q. Sun, W. Luo, Y.-J. Zhang, L.-S. Liao and M.-K. Fung, *J. Mater. Chem. C*, 2019, **7**, 4344–4349.

4 J. Miao and F. Zhang, *J. Mater. Chem. C*, 2019, **7**, 1741–1791.

5 C. M. Raghavan, T.-P. Chen, S.-S. Li, W.-L. Chen, C.-Y. Lo, Y.-M. Liao, G. Haider, C.-C. Lin, C.-C. Chen, R. Sankar, Y.-M. Chang, F.-C. Chou and C.-W. Chen, *Nano Lett.*, 2018, **18**, 3221–3228.

6 Y. Wang, Y. Zhang, P. Zhang and W. Zhang, *Phys. Chem. Chem. Phys.*, 2015, **17**, 11516–11520.

7 S. De Wolf, J. Holovsky, S.-J. Moon, P. Löper, B. Niesen, M. Ledinsky, F.-J. Haug, J.-H. Yum and C. Ballif, *J. Phys. Chem. Lett.*, 2014, **5**, 1035–1039.

8 C. M. Sutter-Fella, Y. Li, M. Amani, J. W. Ager, F. M. Toma, E. Yablonovitch, I. D. Sharp and A. Javey, *Nano Lett.*, 2016, **16**, 800–806.

9 G. Xing, N. Mathews, S. Sun, S. S. Lim, Y. M. Lam, M. Grätzel, S. Mhaisalkar and T. C. Sum, *Science*, 2013, **342**, 344–347.

10 K. X. Steirer, P. Schulz, G. Teeter, V. Stevanovic, M. Yang, K. Zhu and J. J. Berry, *ACS Energy Lett.*, 2016, **1**, 360–366.

11 S. Mahajan, W. D. Johnston, M. A. Pollack and R. E. Nahory, *Appl. Phys. Lett.*, 1979, **34**, 717–719.

12 Y. Rakita, I. Lubomirsky and D. Cahen, *Mater. Horiz.*, 2019, **6**, 1297–1305.

13 F. Jiang, X. Jiang, W. Zheng, Y. Ouyang, Y. Zhang, L. Li, P. Fan, H. Zhao, Y. Li, Y. Jiang, X. Zhu, X. Zhuang, Y.-X. Feng and A. Pan, *J. Mater. Chem. C*, 2020, **8**, 13976–13981.

14 D. Weber, *Zeitschrift für Naturforsch. B*, 1978, **33**, 1443–1445.

15 Y. Dang, Y. Liu, Y. Sun, D. Yuan, X. Liu, W. Lu, G. Liu, H. Xia and X. Tao, *CrystEngComm*, 2015, **17**, 665–670.

16 P. Nandi, C. Giri, B. Joseph, S. Rath, U. Manju and D. Topwal, *J. Phys. Chem. A*, 2016, **120**, 9732–9739.

17 Z. Lian, Q. Yan, Q. Lv, Y. Wang, L. Liu, L. Zhang, S. Pan, Q. Li, L. Wang and J.-L. Sun, *Sci. Rep.*, 2015, **5**, 16563.

18 M. I. Saidaminov, A. L. Abdelhady, B. Murali, E. Alarousu, V. M. Burlakov, W. Peng, I. Dursun, L. Wang, Y. He, G. Maculan, A. Goriely, T. Wu, O. F. Mohammed and O. M. Bakr, *Nat. Commun.*, 2015, **6**, 7586.

19 A. A. Zhumekenov, M. I. Saidaminov, M. A. Haque, E. Alarousu, S. P. Sarmah, B. Murali, I. Dursun, X.-H. Miao, A. L. Abdelhady, T. Wu, O. F. Mohammed and O. M. Bakr, *ACS Energy Lett.*, 2016, **1**, 32–37.

20 G. Maculan, A. D. Sheikh, A. L. Abdelhady, M. I. Saidaminov, M. A. Haque, B. Murali, E. Alarousu, O. F. Mohammed, T. Wu and O. M. Bakr, *J. Phys. Chem. Lett.*, 2015, **6**, 3781–3786.

21 Y. Zhang, Y. Liu, Y. Li, Z. Yang and S. (Frank) Liu, *J. Mater. Chem. C*, 2016, **4**, 9172–9178.

22 P. Nandi, C. Giri, D. Swain, U. Manju, S. D. Mahanti and D. Topwal, *ACS Appl. Energy Mater.*, 2018, **1**, 3807–3814.

23 Y. Liu, Z. Yang, D. Cui, X. Ren, J. Sun, X. Liu, J. Zhang, Q. Wei, H. Fan, F. Yu, X. Zhang, C. Zhao and S. (Frank) Liu, *Adv. Mater.*, 2015, **27**, 5176–5183.

24 H.-S. Rao, W.-G. Li, B.-X. Chen, D.-B. Kuang and C.-Y. Su, *Adv. Mater.*, 2017, **29**, 1602639.

25 D. Shi, V. Adinolfi, R. Comin, M. Yuan, E. Alarousu, A. Buin, Y. Chen, S. Hoogland, A. Rothenberger, K. Katsiev, Y. Losovyj, X. Zhang, P. A. Dowben, O. F. Mohammed, E. H. Sargent and O. M. Bakr, *Science*, 2015, **347**, 519 LP–522.

26 N. J. Jeon, J. H. Noh, Y. C. Kim, W. S. Yang, S. Ryu and S. Il Seok, *Nat. Mater.*, 2014, **13**, 897–903.

27 P. Nandi, C. Giri, U. Bansode and D. Topwal, *AIP Conf. Proc.*, 2017, **1832**, 80065.

28 D. Niesner, O. Schuster, M. Wilhelm, I. Levchuk, A. Osvet, S. Shrestha, M. Batentschuk, C. Brabec and T. Fauster, *Phys. Rev. B*, 2017, **95**, 75207.

29 C. Wang, B. R. Ecker, H. Wei, J. Huang, J.-Q. Meng and Y. Gao, *Phys. Chem. Chem. Phys.*, 2017, **19**, 5361–5365.

30 P. Nandi, S. K. Pandey, C. Giri, V. Singh, L. Petaccia, U. Manju, S. D. Mahanti and D. Topwal, *J. Phys. Chem. Lett.*, 2020, **11**, 5719–5727.

31 M. D. Smith, A. Jaffe, E. R. Dohner, A. M. Lindenberg and H. I. Karunadasa, *Chem. Sci.*, 2017, **8**, 4497–4504.

32 Q. Li, Z. Chen, B. Yang, L. Tan, B. Xu, J. Han, Y. Zhao, J. Tang and Z. Quan, *J. Am. Chem. Soc.*, 2020, **142**, 1786–1791.

33 Z. Yang, X. Wang, Y. Chen, Z. Zheng, Z. Chen, W. Xu, W. Liu, Y. (Michael) Yang, J. Zhao, T. Chen and H. Zhu, *Nat. Commun.*, 2019, **10**, 4540.
34 S. Kahmann, E. K. Tekelenburg, H. Duim, M. E. Kamminga and M. A. Loi, *Nat. Commun.*, 2020, **11**, 2344.
35 L. Zhou, J.-F. Liao, Z.-G. Huang, J.-H. Wei, X.-D. Wang, W.-G. Li, H.-Y. Chen, D.-B. Kuang and C.-Y. Su, *Angew. Chem., Int. Ed.*, 2019, **58**, 5277–5281.
36 L. Zhou, J.-F. Liao, Z.-G. Huang, J.-H. Wei, X.-D. Wang, H.-Y. Chen and D.-B. Kuang, *Angew. Chem., Int. Ed.*, 2019, **58**, 15435–15440.
37 J. Zhou, M. Li, L. Ning, R. Zhang, M. S. Molokeev, J. Zhao, S. Yang, K. Han and Z. Xia, *J. Phys. Chem. Lett.*, 2019, **10**, 1337–1341.
38 P. Nandi, D. Topwal, N.-G. Park and H. Shin, *J. Phys. D: Appl. Phys.*, 2020, **53**, 493002.
39 P. Nandi, C. Giri, D. Swain, U. Manju and D. Topwal, *CrystEngComm*, 2019, **21**, 656–661.
40 H. Mashiyama, Y. Kurihara and T. Azetsu, *J. Korean Phy. Soc.*, 1998, **32**, S156–S158.
41 Y. Yang, Y. Yan, M. Yang, S. Choi, K. Zhu, J. M. Luther and M. C. Beard, *Nat. Commun.*, 2015, **6**, 7961.
42 D. Priante, I. Dursun, M. S. Alias, D. Shi, V. A. Melnikov, T. K. Ng, O. F. Mohammed, O. M. Bakr and B. S. Ooi, *Appl. Phys. Lett.*, 2015, **106**, 081902.
43 M. I. Dar, G. Jacopin, S. Meloni, A. Mattoni, N. Arora, A. Boziki, S. M. Zakeeruddin, U. Rothlisberger and M. Grätzel, *Sci. Adv.*, 2016, **2**, e1601156.
44 J. Fu, N. F. Jamaludin, B. Wu, M. Li, A. Solanki, Y. F. Ng, S. Mhaisalkar, C. H. A. Huan and T. C. Sum, *Adv. Energy Mater.*, 2019, **9**, 1803119.
45 Y. P. Varshni, *Physica*, 1967, **34**, 149–154.
46 P. Nandi, P. Madadevan and D. Topwal, Unpubl. result.
47 S. Sarkar and P. Mahadevan, *Phys. Rev. B*, 2017, **95**, 214118.
48 E. R. Dohner, E. T. Hoke and H. I. Karunadasa, *J. Am. Chem. Soc.*, 2014, **136**, 1718–1721.
49 E. R. Dohner, A. Jaffe, L. R. Bradshaw and H. I. Karunadasa, *J. Am. Chem. Soc.*, 2014, **136**, 13154–13157.
50 M. Cong, B. Yang, F. Hong, T. Zheng, Y. Sang, J. Guo, S. Yang and K. Han, *Sci. Bull.*, 2020, **65**, 1078–1084.
51 R. Zeng, L. Zhang, Y. Xue, B. Ke, Z. Zhao, D. Huang, Q. Wei, W. Zhou and B. Zou, *J. Phys. Chem. Lett.*, 2020, **11**, 2053–2061.
52 S. Li, J. Luo, J. Liu and J. Tang, *J. Phys. Chem. Lett.*, 2019, **10**, 1999–2007.
53 J. Shi, Y. Li, J. Wu, H. Wu, Y. Luo, D. Li, J. J. Jasieniak and Q. Meng, *Adv. Opt. Mater.*, 2020, **8**, 1902026.
54 R. Wang, J. Yang, X. Wu and S. Wang, *Nanoscale*, 2016, **8**, 8210–8219.
55 T. Shi, W.-J. Yin, F. Hong, K. Zhu and Y. Yan, *Appl. Phys. Lett.*, 2015, **106**, 103902.
56 Y. Liu, K. Palotas, X. Yuan, T. Hou, H. Lin, Y. Li and S.-T. Lee, *ACS Nano*, 2017, **11**, 2060–2065.
57 D. J. Vogel, T. M. Inerbaev and D. S. Kilin, *J. Phys. Chem. C*, 2018, **122**, 5216–5226.
58 X. Zhu, H. Su, R. A. Marcus and M. E. Michel-Beyerle, *J. Phys. Chem. Lett.*, 2014, **5**, 3061–3065.
59 S. Zou, Z. Gong, B. Liang, L. Hou, R. Liu, H. Zhong, B. Zou and A. V. Kavokin, *J. Phys. Commun.*, 2017, **1**, 55018.
60 M. Hirasawa, T. Ishihara, T. Goto, K. Uchida and N. Miura, *Phys. B*, 1994, **201**, 427–430.
61 A. Milev, D. M. A. S. Dissanayake, G. S. K. Kannangara and A. R. Kumarasinghe, *Phys. Chem. Chem. Phys.*, 2013, **15**, 16294–16302.
62 R. R. Nair, M. Sepioni, I.-L. Tsai, O. Lehtinen, J. Keinonen, A. V. Krasheninnikov, T. Thomson, A. K. Geim and I. V. Grigorieva, *Nat. Phys.*, 2012, **8**, 199–202.
63 G. Z. Xing, Y. H. Lu, Y. F. Tian, J. B. Yi, C. C. Lim, Y. F. Li, G. P. Li, D. D. Wang, B. Yao, J. Ding, Y. P. Feng and T. Wu, *AIP Adv.*, 2011, **1**, 22152.
64 S. Sil, H. Luitel, J. Dhar, M. Chakrabarti, P. P. Ray, B. Bandyopadhyay and D. Sanyal, *Phys. Lett. A*, 2020, **384**, 126278.
65 B. Náfrádi, P. Szirmai, M. Spina, H. Lee, O. V. Yazyev, A. Arakcheeva, D. Chernyshov, M. Gibert, L. Forró and E. Horváth, *Nat. Commun.*, 2016, **7**, 13406.